GEOPHYSICS, VOL. 71, NO. 2 (MARCH-APRIL 2006); P. G43–G51, 11 FIGS., 1 TABLE.
10.1190/1.2187748

Mapping thin resistors and hydrocarbons with marine EM methods: Insights from 1D modeling

Steven Constable[1] and Chester J. Weiss[2]

ABSTRACT

The use of marine controlled-source electromagnetic EM (CSEM) sounding to detect thin resistive layers at depths below the seafloor has been exploited recently to assess the resistivity of potential hydrocarbon reservoirs before drilling. We examine the sensitivity of the CSEM method to such layers with forward and inverse modeling in one and three dimensions. The 3D modeling demonstrates that if both source and receivers are over a tabular 3D target, 1D modeling predicts the observed response to very high accuracy. Experimental design can thus be based on 1D analysis in which hundreds of range and frequency combinations can be computed to find the optimal survey parameters for a given target structure. Modeling in three dimensions shows that the vertical electric-field response is largest over the edges of a 3D target. The 3D modeling also suggests that a target body needs to have a diameter twice the burial depth to be reliably seen by CSEM sounding. A simple air-wave model (energy propagating from source to receiver via the atmosphere) allows the effects of the target layer and atmosphere to be separated and shows where sensitivity to the target is diminished or lost because of finite water depth as a function of range, frequency, and seafloor resistivity. Unlike DC resistivity sounding, the marine CSEM method is not completely T-equivalent and, in principle, can resolve resistivity and thickness separately. Smooth inversion provides an estimate of the method's resolving power and highlights the fact that although the radial CSEM fields contain most of the sensitivity to the thin resistive target, inverted alone they produce only increasing resistivity with depth. Inclusion of the radial mode CSEM data forces the recovery of the thin resistor, but magnetotelluric data can be used more effectively to achieve the same result.

INTRODUCTION

Electrical resistivity provides important information on the porosity and pore geometry of geologic formations as well as the nature of the fluids that fill pore spaces. For these reasons, borehole resistivity logs are a standard commodity in hydrocarbon exploration. There are two basic methods of estimating formation resistivity without the use of boreholes: magnetotelluric (MT) and controlled-source electromagnetic (CSEM) sounding. Both approaches can be applied to marine exploration with appropriate modifications to instrumentation and methodology (Figure 1).

For the MT method, the frequency-domain transfer function between recordings of magnetic and electric fields provides an electromagnetic impedance of the seafloor beneath the recording site. The application to the marine environment is mostly an issue of instrumentation because if lateral variations in resistivity are not significant (rarely, the case because of the ubiquity of coastlines), then the effect of the overlying water can be neglected in the processing and interpretation of a seafloor MT site. Although Cagniard (1953) initially considered the possibility of carrying out marine measurements in his proposal for the MT method, the first seafloor MT study in which both electric and magnetic measurements were made appears to have been in 1973, reported by Cox et al. (1980). Because the conductive (0.3 Ωm) seawater attenuates MT source fields at periods shorter than a few thousand seconds on the deep seafloor, marine MT traditionally utilizes long-period instrumentation. Attempts to adapt commercial broadband land MT equipment to shallow-water marine exploration (Hoehn and Warner, 1983) were hampered by the bulk of the early land equipment and the noisy environment of shallow water. More recent improvements in instrumentation (Constable et al., 1998) have made the collection of continental shelf marine MT data in the band 1 s to 3,000 s a matter of routine in water 100-m to 4,000-m deep.

The horizontal electric-dipole marine-controlled CSEM method was originally developed for deepwater studies of the

Manuscript received by the Editor December 1, 2004; revised manuscript received June 28, 2005; published online March 9, 2006.
[1]Scripps Institution of Oceanography, La Jolla, California 92093-0225. E-mail: sconstable@ucsd.edu.
[2]Sandia National Laboratories, P. O. Box 5800 MS-0750, Albuquerque, New Mexico 87185. E-mail: cjweiss@sandia.gov.

oceanic lithosphere (Cox, 1981), and first experiments were carried out in 1979 (Spiess et al., 1980). The relatively high-frequency energy lost to the MT method at the seafloor is replaced by a dipolar deep-towed transmitter, and seafloor receivers measure electric fields as a function of transmitter-receiver range and frequency. Academic applications of this method have included the study of the oceanic lithosphere (e.g., Constable and Cox, 1996), midocean ridges (MacGregor et al., 2001), and seafloor gas hydrates (e.g., Yuan and Edwards, 2000). Early proposals to use the method for petroleum exploration (e.g., Chave et al., 1991), similar to early MT efforts, concentrated on relatively shallow water and exploration targets. With the migration of hydrocarbon exploration into the deeper waters of the continental slopes, marine CSEM recently has become an important exploration tool for the hydrocarbon industry (e.g., MacGregor and Sinha, 2000; Ellingsrud et al., 2002; Eidsmo et al., 2002; Kong et al., 2002; Johansen et al., 2005).

In this paper we examine the sensitivity of marine EM methods (mainly CSEM, but we consider also the role of MT) to thin resistive layers buried in conductive media. This model represents an oil or gas reservoir in water-saturated sediments, but the reader is cautioned that it also may represent any thin, resistive lithological horizon of low porosity such as a volcanic sill, evaporite, or carbonate.

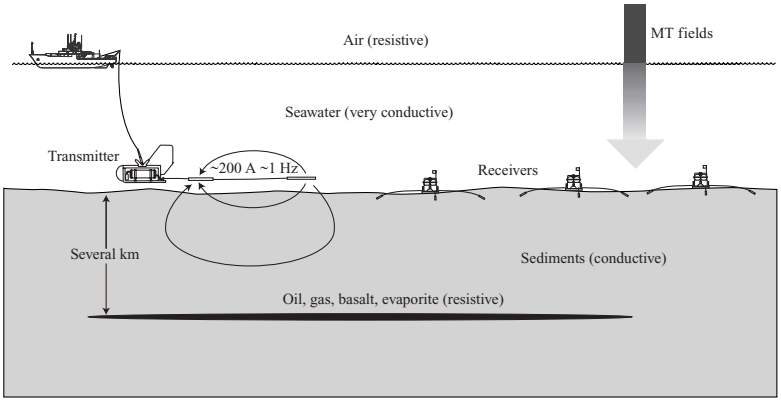

Figure 1. Conceptual diagram of the marine CSEM method. A deep-towed transmitter close to the seafloor injects a current of several hundred amps into the seawater from an electric dipole, creating magnetic and electric fields that propagate diffusively into the seafloor. Electric dipole receivers record the seafloor electric fields at various ranges from the transmitter. When equipped with additional magnetic field sensors, the same receivers can record magnetotelluric signals.

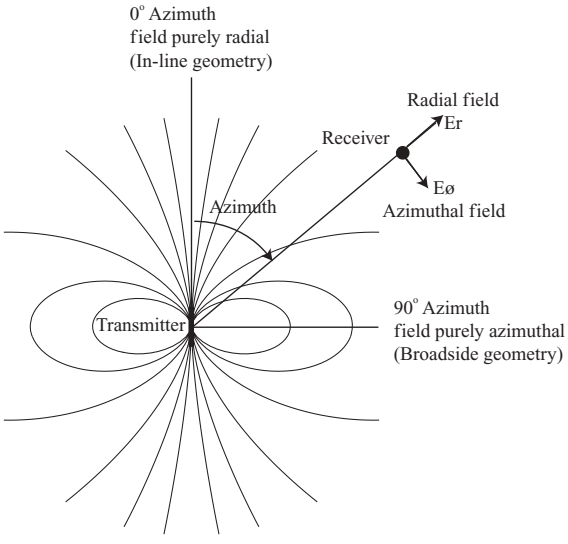

Figure 2. The geometry of CSEM dipole fields. Along the polar axis of the dipole transmitter, the field is purely radial. Along the equatorial axis, the field is purely azimuthal. At other azimuths the received fields are a trigononmetric mix of both modes.

THE 1D RESPONSE OF A THIN RESISTIVE LAYER

We have long known that the marine CSEM method is preferentially sensitive to thin resistive layers (Constable et al., 1986; Cheesman et al., 1987), thus making the method possibly useful for assessing the resistivity of potential drilling targets (Eidsmo et al., 2002). Electric-field amplitudes and phases can be described in terms of radial and azimuthal modes with respect to transmitter orientation. Figure 2 defines these geometries. Figure 3 illustrates the sensitivity to thin layers by plotting the radial and azimuthal response of a canonical model consisting of a 100-m thick reservoir buried at a depth of 1000 m in 1 km seawater.

Our calculations use the 1D code of Flosadottir and Constable (1996), which combines Anderson's (1989) fast Hankel transform with Chave and Cox's (1982) kernel function evaluations, in this case, using a transmission frequency of 1 Hz. The amplitude plots show the electric-field magnitudes as a function of transmitter–receiver offset for the canonical model, a half-space of 1 Ωm resistivity (i.e., sediments without a reservoir layer), and the component of the received energy that has propagated through the atmosphere. The latter, discussed more below, illustrates which parts of the model and half-space responses are associated with the seafloor and which parts are associated with the atmosphere. On the phase plots, we show only the response of the model and half-space; the effect of the atmosphere is clearly evident as a constant phase of ~400°. The dip in amplitude and phase — as the model and half-space curves intersect the so-called air-wave curve — presumably results from interaction at the seafloor of energy with similar magnitude but different phase from the two propagation paths.

Phase and amplitude respond in similar ways to 1D subseafloor structure and probably to 3D subseafloor structure as well. That is, part of the model that does not produce an amplitude response will not produce a phase response and vice versa. Furthermore, errors in processed in-phase and out-of-phase components will propagate into both amplitude and phase estimates. Indeed, timing errors in the transmitter or receiver will degrade phase data but not amplitudes. However, it is possible that galvanic distortions associated with resistivity heterogeneity near the transmitter or receivers will have less effect on phase than amplitude, as is the case with land MT.

Because CSEM field amplitudes vary over such a large range, it is useful to consider fields normalized by the (half-space) response. In Figure 3 the normalized fields show that the radial amplitudes are 20 times more sensitive to the presence of the thin resistive layer than the azimuthal fields. This is because the radial dipole geometry includes a vertical component of electric current, which is interrupted by the thin resistor, whereas the azimuthal dipole fields are largely horizontal and perturbed little by the presence of the thin inhomogeneity, noted previously by Eidsmo et al. (2002). Although not shown here, the MT method, which depends on induced electric fields that are largely horizontal, is similarly blind to the existence of thin resistive layers.

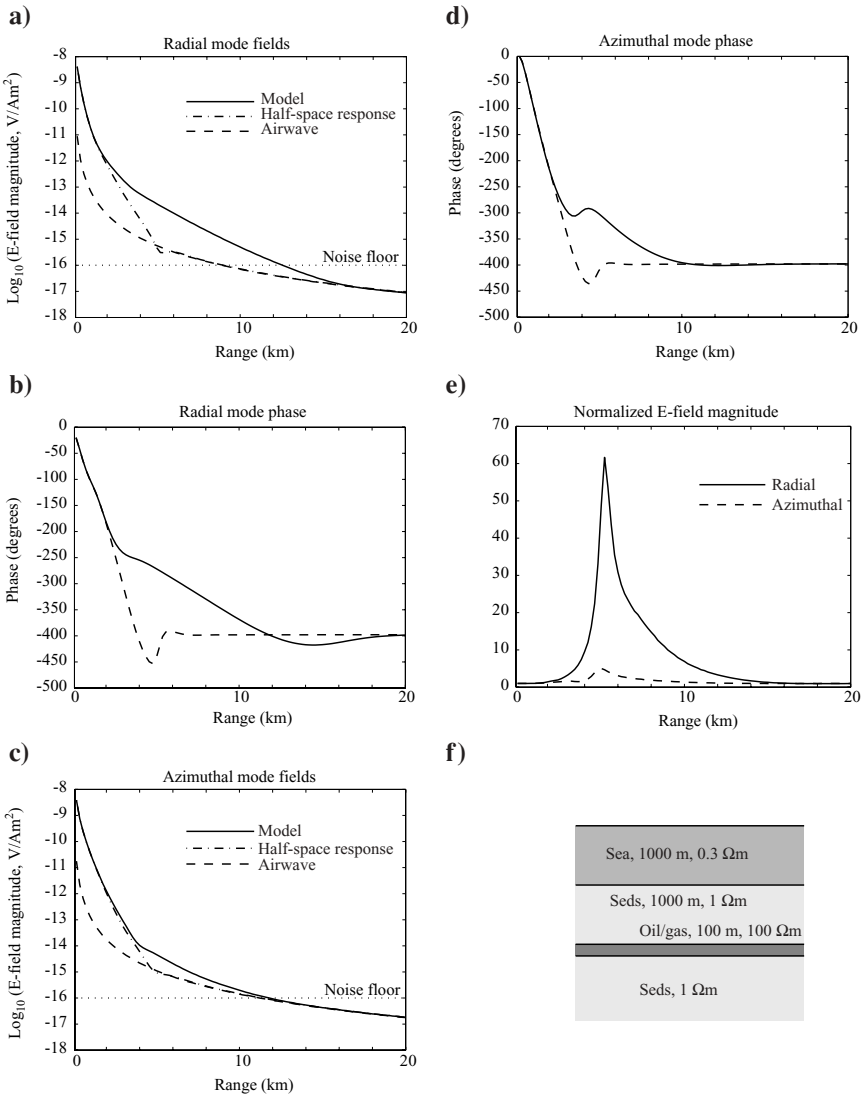

Figure 3. (a, b) Radial and (c, d) azimuthal mode CSEM amplitudes and phases as a function of source–receiver range at a frequency of 1 Hz, calculated for the model shown in (f) with (model) and without (half-space) the thin resistive layer. In (e) we show the radial and azimuthal field amplitudes normalized by the response of the half-space.

THE 3D RESPONSE OF A THIN RESISTIVE LAYER

Below we use 1D forward and inverse modeling to examine further the sensitivity of the CSEM and MT methods to thin resistive layers, but first we introduce a simple 3D calculation to show that when the transmitter and receiver are both over the target of interest, insights obtained from 1D calculations are appropriate. Figure 4 shows the radial mode electric-field amplitudes and phases for a buried disk of various diameters. The calculations are carried out using the finite-difference code of Weiss (2001), modified to include the horizontal dipole source. The thickness, depth, and resistivity of the disk and the resistivity of the host medium are the same as those of our canonical model; only the disk diameter varies. The transmitter is positioned over one edge of the disk, and the electric fields are plotted along a line passing from the transmitter, through the point over the center of the disk, and across the far edge.

Calculations for disk diameters of 2 km and 5 km are shown. An infinite disk is represented by the 1D layered calculations introduced above, as is a zero-diameter disk, which is represented by a half-space calculation using the 1D code. We see that for the 5-km disk, both the amplitude and phase of the electric fields are identical to the 1D layered calculation until the receiver is positioned directly over the disk edge. The fields then fall away rapidly at the same attenuation rate as for the half-space. The 2-km diameter disk is perhaps the smallest that reliably could be seen using this method, differing from the half-space calculations by approximately 50% in amplitude and about 20° in phase. This suggests that a target such as this must be at least twice its burial depth in lateral extent before it is visible to the CSEM method.

The agreement between the 1D and 3D calculations not only verifies the accuracy of the 3D code, but also shows that while the transmitter and receiver are both over a tabular target, 1D modeling is highly accurate. This is because the EM fields from the transmitter decay rapidly, a combination of a $1/r^3$ dipole geometry and the exponential inductive attenuation. Therefore, the contribution from structure that is distant from the transmitter-receiver region is very small. This is in stark contrast to the MT method, in which the EM source field extends globally and can generate galvanic effects from structure far from the observation site. In addition to being geometrically compact, most of the galvanic effects associated with the CSEM response of the thin target are generated on the upper and lower surfaces, whereas in MT, galvanic effects are predominantly horizontal and produce laterally extensive electric fields.

Clearly, the agreement between one and three dimensions does not diminish the importance of 3D modeling in data interpretation and experimental design where the target's lateral extent is important. However, it does show that simple experimental design considerations such as frequency, range, and detectability can largely be addressed using 1D codes, which allow a vastly larger number of models and experimental parameters to be assessed. Furthermore, comprehensive studies consisting of many inversion runs of synthetic data are currently only practical using 1D methodology.

VERTICAL ELECTRIC-FIELD RESPONSE

One exception of 1D modeling to understand the behavior of the CSEM method is the role of the vertical electric field. In Figure 5, we plot the vertical electric field generated by a horizontal dipole transmitter over the disk models. The vertical field responds only to the edge of the disks, while the 5-km radius disk produces a significant response in the horizontal fields at a range of about 2500 m. We do not see similar response in the vertical fields until we reach a range more than 4000 m and the edge of the structure. Vertical field CSEM data thus have potential for illuminating the edge of hydrocarbon structures. Although we have not modeled it, reciprocity suggests that the same effect can be achieved with a vertical transmitter and horizontal field receivers.

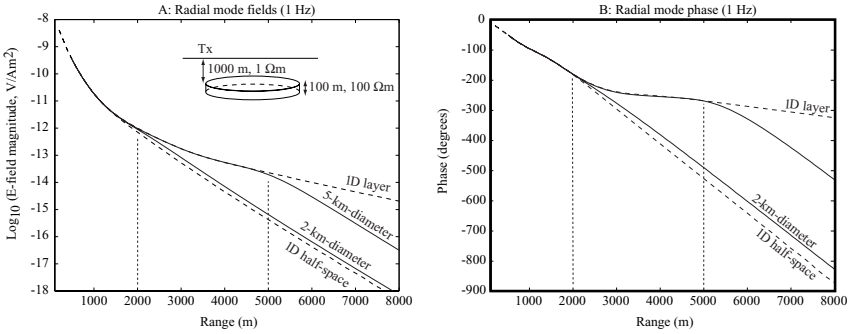

Figure 4. (a) Electric-field amplitude and (b) phase for a buried disk of various diameters. There is no air layer in this model (i. e., the ocean is considered arbitrarily deep).

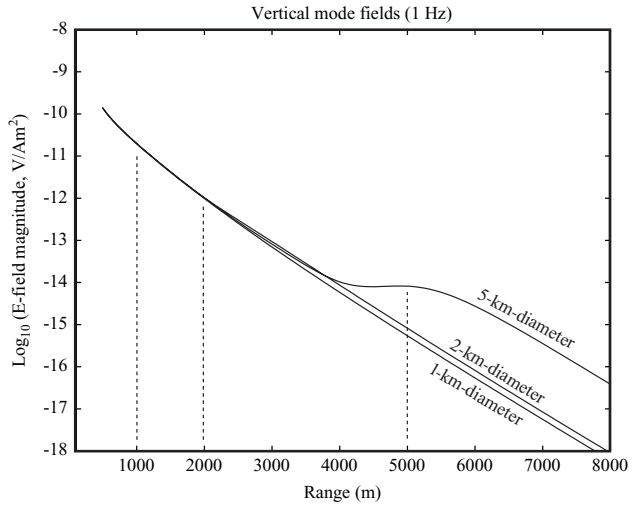

Figure 5. Vertical electric-field amplitude for a buried disk of various diameters.

PROPAGATION THROUGH THE ATMOSPHERE

We can understand more fully the effect of the atmosphere on the seafloor CSEM response by separating the components of energy that propagate though the seawater/seabed and the atmosphere (which we call the *air wave,* for brevity). We can estimate the double half-space response (seawater and seabed) or a more complicated model by running the 1D forward code with a large water depth. While this code models the effect of the air on propagation and could be run a second time to show the effect of including the air layer, we note that a good approximation of the amplitude of the radial mode airwave is

$$E_{\text{air}} = \frac{e^{-2h/\delta}}{2\pi\sigma r^3}$$

where h is water depth, $\delta = \sqrt{2/\sigma\omega\mu_o}$ is the skin depth in seawater of conductivity σ and permeability μ_o at frequency ω, and r is the source-receiver range. This expression is derived from equation 14 of Bannister (1984), but could be thought of as skin-depth attenuation up ($e^{-h/\delta}$) and down ($e^{-h/\delta}$) through the water column, coupled with the $1/r^3$ geometric spreading associated with a dipole. Using this formula, we can demonstrate the behavior of the air wave independently of seafloor resistivity.

In Figure 6, we plot separately the contributions to the horizontal electric-field magnitude from the seafloor and the atmosphere for various water depths and seafloor resistivity. The slope of the propagation through the atmosphere is given only by the $1/r^3$ geometric spreading, but we determine the amplitude by the water depth, which decreases as the water gets deeper and the attenuation more severe. At short ranges the amplitude of the electric field propagating through the seafloor and seawater is similarly given by the $1/r^3$ dipole decay and the resistivity of seawater, but at ranges greater than 1 km, exponential skin-depth attenuation in the seafloor rocks dominates the curves. A more resistive seafloor with larger skin depth supports large electric fields to greater source–receiver ranges.

It can thus be seen that as the seafloor gets more resistive and the seawater gets deeper, the seafloor signal dominates the atmosphere signal to longer ranges. At the range at which the curves cross for a given water depth and seafloor resistivity, the air wave starts to dominate the signal observed on the seafloor. Thus, the curves for a 1 Ωm seafloor and 900-m water depth cross at a range of 4500 m. Because the seafloor signal attenuates much more rapidly than the air wave, by the time this range has doubled the air wave energy is more than 1000 times larger than the seafloor signal. Various schemes have been proposed to separate the air wave from the seafloor signal in the vicinity of the crossover (e.g., Røsten and Amundsen, 2004). The simplest of these is just to include the air layer

in the modeling and interpretation. Johansen et al. (2005) have shown that with a large deeply buried (1100 m) target, in 350-m water depth a signal amounting to a factor of 3 or 4 in electric-field amplitude may be measured in real data before the air wave dominates. In that study, at the 0.25-Hz transmission frequency the seawater was 0.6-skin-depths thick, and the 1.4-Ωm overburden was 1.2-skin-depths thick, and so the air wave was not yet totally dominant.

It is difficult to see that seafloor data of sufficient precision can be collected to extend the effective source — receiver range significantly beyond the transition region — or to extend the operational water depth to areas where the atmosphere is much closer to the receiver (measured as skin depths in seawater) than is the target of interest (measured as skin depths in seafloor host rock). Ultimately, in very shallow water one is effectively operating in an environment that is more similar to working on land than the deep ocean. Thus, the strategy to deal with the air wave is to operate in the time domain rather than frequency domain as Wright et al. (2001) did for mapping a gas reservoir in France.

EFFECTS OF FREQUENCY AND RANGE

In Figure 3, we show the normalized radial field as a function of source–receiver range for a 1-Hz transmission. The normalized fields also depend on frequency and are larger for higher frequencies. However, at higher frequency the magnitude of the fields falls below the instrument noise threshold. An easy way to assess the tradeoff for a given target structure is to contour normalized field versus range and frequency, as we do in Figure 7 for our canonical model. We overlay contours of the magnitudes of the received fields so that regions below the noise threshold of the instrument system can be identified. The strategy in designing an experiment or survey is to make the normalized field as large as possible for the shortest possible range (to increase lateral resolution) while maintaining an adequate signal-to-noise ratio. For example, with an instrument noise floor of 10^{-16}V/(Am^2) and a required SNR of 30, we might choose a frequency of about 3 Hz. This would provide a signal from the target structure that is a factor of 10 above background at a range of about 3.5 km and an electric field that is several hundred times bigger than background at a range of 5 km.

The target structure is seen over a limited range of frequency and source–receiver offset. Frequencies below about 0.2 Hz do not produce large effects because there is little induction in the target layer, and large electric fields are dominated by the water and sediment. At frequencies above 25 Hz, skin depth in the sediments is only 100 m, and most energy is absorbed in the seawater and overburden. At ranges shorter than 2.5 km, the target is too deep (1 km) for the region sampled by the source–receiver geometry. At ranges larger than 15 km, the dominance of the air wave removes any sensitivity to the target.

This approach to experimental design provides an excellent way to ensure that surveys are carried out using frequencies that are appropriate for a given target depth (often estimated from seismic data). However, it does not ensure that sufficient data are collected to distinguish between shallow and deep targets or that other variations in host resistivity can be distinguished from the deeper target. For these reasons, other frequencies — and perhaps other data such as MT — may need to be collected.

NOISE FLOOR OF INSTRUMENT SYSTEMS

Clearly, the noise floor of the transmitter/receiver system plays an important role in survey design. Sources of noise in the receiver instruments include amplifiers, electrodes, water motion, instrument motion, and the magnetotelluric signal.

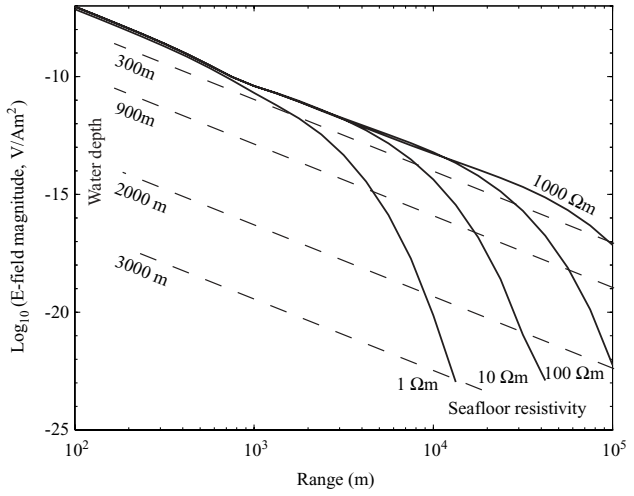

Figure 6. Seafloor 1 Hz CSEM horizontal radial electric-field amplitudes as a function of range and half-space resistivity (solid lines) in the absence of an air layer and the contribution of the electric field that has propagated through the atmosphere (broken lines) for various water depths between 300 m and 3000 m.

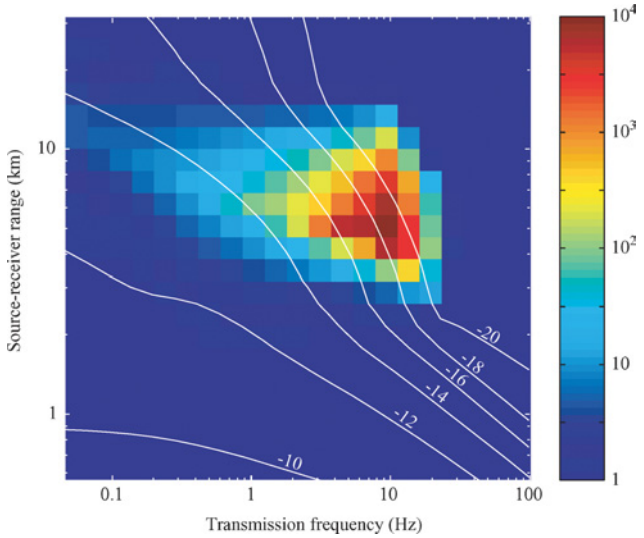

Figure 7. Ratio of the radial horizontal electric-field response of the canonical model to the half-space response as a function of range and frequency. White contour lines show base 10 logarithms of the magnitude of the electric field of the canonical model. The best possible noise floor of current instrument systems is about 10^{-16} V/(Am^2).

Signal increases with the transmitter source dipole moment (SDM), stacking bandwidth, and the length of the receiver antennae (because most noise sources, with the exception of MT signals, are voltages rather than electric fields). The SDM is the product of the zero-to-peak amplitude of the current at the transmission frequency multiplied by the length of the transmission antenna.

Specification of a single component of the system, such as transmitter current, fails to recognize the importance of the other components, so, for example, variations in receiver noise may easily exceed the range of transmitter SDM that may be attainable. For a receiver voltage noise V_r, receiver dipole length l, and stacking bandwidth B, the electric-field noise floor is given by

$$E_n = \frac{V_r}{e(\mathrm{SDM})\sqrt{B}}.$$

For example, for instruments having a voltage noise of 10^{-9} V$\sqrt{\text{Hz}}$ at 1 Hz (Hoversten et al., 2000) and 10-m antennae, a SDM of 45 kAm and 120-s stacking gives an En of 2×10^{-16} V/(Am^2). Such noise levels can be approached in deep water at higher transmission frequencies, but for the water depths (around 1000 m) and frequencies (around 0.25 Hz) typical of continental shelf exploration, water motion and MT signals lift the noise floor to about an order of magnitude worse than this (Figure 8). Given that commercial transmitters with a SDM of around 200 kAm are feasible, and that MT noise can be predicted and removed from the CSEM data to some extent using remote references, 10^{-16} V/(Am^2) probably represents a reasonable lower bound on what is attainable with current technology.

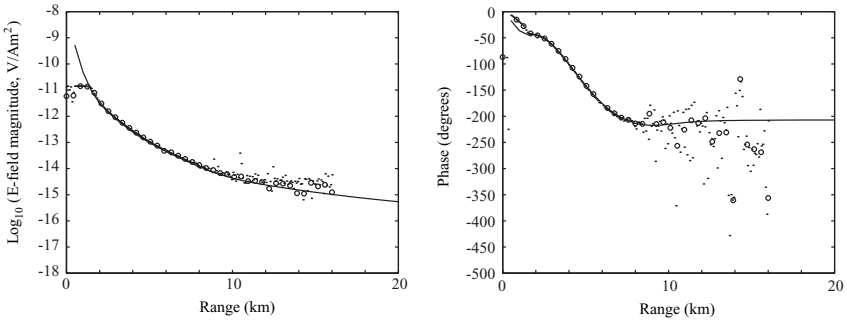

Figure 8. Electric-field amplitude and phase during a test of a 45 kAm transmitter operating at 0.25 Hz in 1130-m water offshore San Diego, U. S. A. The small symbols are 120-s stacks; the larger circles are 600-s stacks. The solid line is a model of 2350-m thick, 1.9-Ωm sediments underlain by resistive basement. The noise floor of about 2×10^{-15} V/(Am^2) is probably caused by MT signals. At ranges less than 1 km, the receiver amplifier is saturated.

EFFECT OF VARYING RESISTIVITY AND TARGET THICKNESS

One possible application of the marine CSEM method is mapping the size (lateral extent and thickness) of hydrocarbon reservoirs. Electromagnetically, there are two contributions to size in the 1D sense — thickness and resistivity — which are correlated inevitably to some extent. In the case of DC resistivity sounding, the tradeoff between resistivity and thickness is almost perfect for a thin resistive layer, and it is only the resistivity–thickness product, or transverse resistance, $T = \rho t$, that is resolved — a phenomenon that is usually called T-equivalence. We investigate these issues for the marine CSEM method; we expect that the galvanic component of current flow will behave as in DC resistivity, and exhibit a T-equivalence, and that the inductive component of field attenuation will be sensitive to the resistivity of the target and, to some extent, be independent of thickness.

Figure 9 shows the effect of reducing only the thickness of our 100-m layer. As one would expect, the electric-field response varies monotonically with thickness. The radial mode response varies almost linearly with thickness, which bodes well for using the method to map reservoir geometry. The azimuthal response is almost zero for layers thinner than 50 m, but again, increases linearly for the thicker layers, albeit at a much smaller rate than for the radial mode.

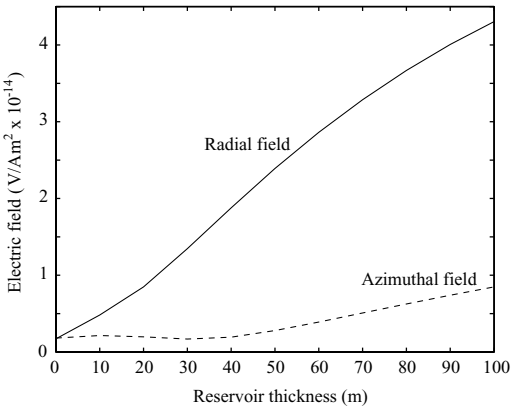

Figure 9. Radial- and azimuthal-field amplitudes at a range of 4.6 km and frequency of 1 Hz for the canonical model as the thickness of the thin resistive layer varies from zero to 100 m.

To study T-equivalence, we increase the resistivity ρ as thickness t is reduced, to keep T invariant. We see from Figure 10 that true T-equivalence is observed only at low frequency (0.1 Hz), and that the relative T-equivalence breaks down progressively as frequency increases (but note that absolute field magnitudes are decreasing with frequency). As the target layer is made thinner at relatively higher frequencies, the normalized response actually gets larger — by 30% in the case of 3 Hz. This suggests that a galvanic response accounts for most, but not all, of the sensitivity to thin resistive layers, and as the resistivity and skin depth increase, there is an increase in inductive response. The implication is that by combining data at different frequencies, thickness and resistivity can be estimated separately.

SYNTHETIC-DATA INVERSION

One measure of resolution is the ability to recover structure by inversion of synthetic data. Regularized smooth inversion,

such as the OCCAM algorithm (Constable et al., 1987), provides an end-member approach to resolution analysis because it assumes no prior structure in the starting model and generates the model with the least structure.

We generated three types of synthetic data from our canonical model: (1) radial mode CSEM data at 20 ranges spaced evenly between 500 m and 10 km with 10% added noise (zero mean Gaussian); (2) azimuthal mode CSEM data at similar ranges with similar noise; and (3) MT apparent resistivity and phase at 20 periods spaced logarithmically between 1.5 s and 2150 s, with 10% error in resistivity and 2.9° error in phase. We inverted these data in four different combinations: (1) radial CSEM data only (E_r), (2) radial and azimuthal CSEM data ($E_r + E\phi$), (3) radial CSEM data with MT data ($MT + E_r$), and (4) the entire data set. The actual data are listed in Table 1. We started all inversions with a featureless half-space of 1 Ωm. The one free variable in the regularized inversion algorithm is the degree of data misfit requested. Because we know what the misfit of the noisy data to the true (starting) model is, we can choose a target misfit accordingly and set this to 1.2 times the actual misfit to the true model response for each of the four data subsets. Figure 11 shows the results.

The E_r only inversion is the most dramatic because it is completely unrepresentative of the starting model, with resistivity increasing steadily with depth from about 1 Ωm to over 10 Ωm. This behavior is somewhat disappointing in view of the forward modeling, which shows that the E_r data contain most of the sensitivity to the resistive layer, and has been observed previously by Eidsmo et al. (2002). The $E\phi$ response to such a thick resistive layer, however, would be larger than is observed, and so inclusion of these data in the inversion ($E_r + E\phi$) forces the model to generate a thinner resistive layer at approximately the right depth. The deeper resistivity is about twice as large as in the starting model because the CSEM data are losing resolution at depth.

Interestingly, the MT data provides the same effect as the $E\phi$ data, in that they too are relatively insensitive to the thin resistive layer but can eliminate the thicker layer as a possibility, and the E_r + MT inversion does as good a job as the $E_r + E\phi$ inversion at recovering the target layer and actually does better at recovering the deeper resistivity because MT has greater sensitivity at depth than CSEM. Inversion of

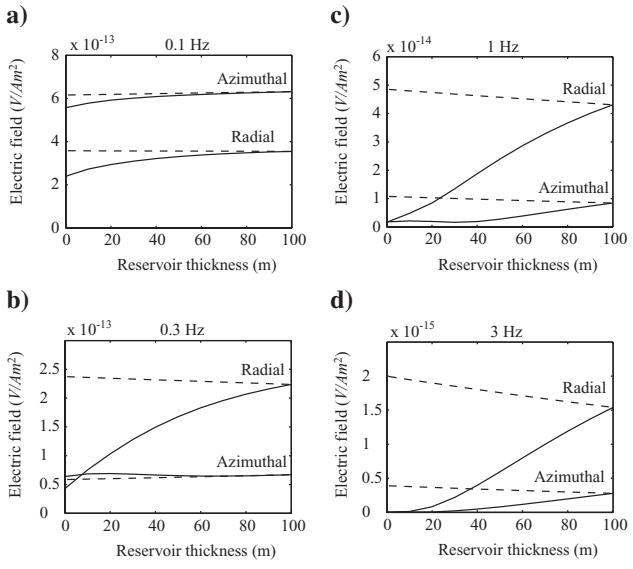

Figure 10. Radial- and azimuthal-field amplitudes at a range of 4.6 km and various frequencies for the canonical model as the thickness of the thin resistive layer is varied from zero to 100 m (solid lines) and when the resistivity is adjusted to maintain a resistivity–thickness product of 10 000 Ωm^2 (broken lines).

Table 1. Data used for inversion study.

CSEM data: Range (m)	$E\rho$ (V/Am^2)	Error (V/Am^2)	$E\phi$ (V/Am^2)	Error (V/Am^2)
500	.307E-09	.307E-10	.396E-09	.396E-10
1000	.193E-10	.193E-11	.474E-10	.474E-11
1500	.309E-11	.309E-12	.671E-11	.671E-12
2000	.115E-11	.115E-12	.142E-11	.142E-12
2500	.370E-12	.370E-13	.376E-12	.376E-13
3000	.190E-12	.190E-13	.908E-13	.908E-14
3500	.852E-13	.852E-14	.288E-13	.288E-14
4000	.500E-13	.500E-14	.920E-14	.920E-15
4500	.309E-13	.309E-14	.700E-14	.700E-15
5000	.204E-13	.204E-14	.425E-14	.425E-15
5500	.162E-13	.162E-14	.314E-14	.314E-15
6000	.104E-13	.104E-14	.225E-14	.225E-15
6500	.632E-14	.632E-15	.131E-14	.131E-15
7000	.513E-14	.513E-15	.754E-15	.754E-16
7500	.230E-14	.230E-15	.704E-15	.704E-16
8000	.215E-14	.21 5E-15	.543E-15	.543E-16
8500	.131E-14	.131E-15	.410E-15	.410E-16
9000	.887E-15	.887E-16	.301E-15	.301E-16
9500	.780E-15	.781E-16	.191E-15	.191E-16
10 000	.388E-15	.388E-16	.209E-15	.209E-16

MT data: Period (s)	ρ_a (Ωm)	Error (Ωm)	Phase (°)	Error (°)
1.47	.948	.0948	43.1	2.90
2.15	.970	.0970	47.3	2.90
3.16	1.14	.114	43.3	2.90
4.64	1.01	.101	46.3	2.90
6.81	1.14	.114	46.2	2.90
10.00	1.04	.104	41.6	2.90
14.68	1.06	.106	45.5	2.90
21.54	1.06	.106	45.4	2.90
31.62	.943	.0943	48.7	2.90
46.42	.941	.0941	49.6	2.90
68.13	1.03	.103	48.9	2.90
100.00	.969	.0969	46.8	2.90
146.78	1.07	.107	46.2	2.90
215.44	1.25	.125	49.2	2.90
316.23	.839	.0839	48.3	2.90
464.16	.896	.0896	45.4	2.90
681.29	.901	.0901	49.2	2.90
1000.00	1.13	.113	44.1	2.90
1467.80	.983	.0983	45.9	2.90
2154.43	.805	.0805	50.7	2.90

the entire data set produces only marginal improvement over the E_r + MT inversion.

The fact that MT data plays a similar role to Eϕ data is of significant practical importance. Collection of MT data during a CSEM survey is almost cost-free, since the seafloor receivers can collect both CSEM and MT data, and MT responses can be processed from data collected when the CSEM transmitter is turned off or out of range. Only a single MT site is needed to constrain the model, although in practice a significant fraction of the CSEM receivers could be used for MT as well. On the other hand, collection of Eϕ data requires extra transmitter tows of appropriate geometry, consuming additional shiptime (usually the most expensive component of the survey) and increasing manpower and equipment costs.

The smoothing regularization produces an oscillation in the model at the top of the large step in target resistivity to approximate this boundary with minimum penalty. The effect of this structure is that the model slightly underestimates the depth to the target layer much the same way anisotropy would. While our purpose is to illustrate the intrinsic resolution of the CSEM and MT methods given no additional information, in practice, an explorer would not rely solely on the smooth inversion for interpretation and probably would know target layer's depth from seismic data and sediment resistivity from nearby well logs. More realistic models that are more realistic in some cases, and thus apparently higher resolution, may be obtained by assuming the existence of sharp boundaries in resistivity (Smith et al., 1999; deGroot-Hedlin and Constable, 2004). This is a reasonable approach as long as one recognizes that the improved resolution comes from a prior assumption that cannot be verified using EM data alone. We demonstrate this here by a three-layer least-squares fit to the entire MT+CSEM data set. This model recovers the depth, thickness, and resistivity of the thin layer to 95% accuracy or better. Ultimately, joint inversion of CSEM and seismic data can be used to constrain reservoir properties such as hydrocarbon saturation (Hoversten et al., personal communication, 2005).

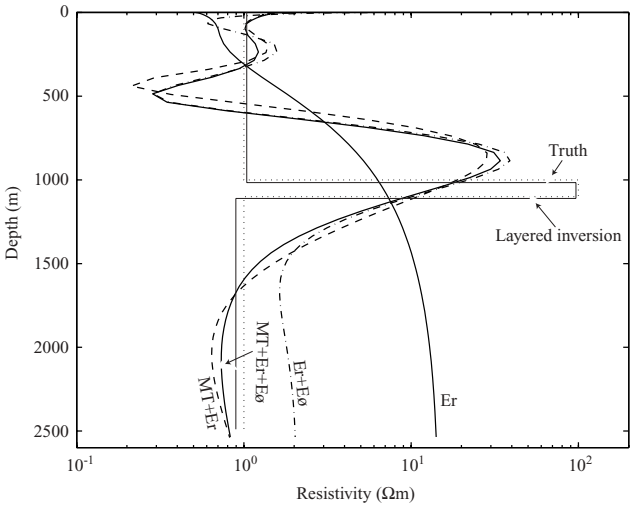

Figure 11. Inversion of synthetic data sets generated by the canonical model, shown here as the broken line labeled *truth*. The E_r is a smooth inversion of only radial mode CSEM data, and E_r + Eϕ is a smooth inversion of both CSEM modes. We also show the results of joint smooth inversion of singlesite MT data with both CSEM data sets (MT+E_r+Eϕ). While the smooth inversions show inherent resolution of the EM methods, if layered structure is assumed a priori, a joint layered inversion of the MT+E_r+Eϕ data set (solid line) almost recovers the starting model.

CONCLUSIONS

Although 3D modeling will be important in the interpretation of large CSEM and MT data sets over targets of complicated geometry, simpler 1D modeling can be used reliably to design the survey parameters, given information such as sediment resistivity, water depth, and target depth. Because the marine CSEM method is not completely T-equivalent, particularly at higher frequencies where inductive effects are greatest, reservoir thickness and resistivity can be estimated as separate parameters. However, inversion of EM data without constraints or prior structural information will be limited by the intrinsically smooth resolution kernels and, in particular, the radial mode CSEM data, which otherwise carries most of the information about the target structure, requires the inclusion of azimuthal mode CSEM data, or, more economically, MT data, to recover even a smooth version of the target structure.

ACKNOWLEDGMENTS

The authors thank Kerry Key and James Behrens for comments on the manuscript. The authors also thank the reviewers, and particularly David Alumbaugh, who drew our attention to the Bannister reference. Funding for this work was provided by RPSEA and the Scripps Institution of Oceanography Seafloor Electromagnetic Methods Consortium. Portions of this work were completed at Sandia National Laboratories, Albuquerque, New Mexico. Sandia is a multiprogram laboratory operated by Sandia Corporation, a Lockheed Martin Company, for the United States Department of Energy's National Nuclear Security Administration under contract DE-AC04-94AL85000.

REFERENCES

Anderson, W. L., 1989, A hybrid fast Hankel transform algorithm for electromagnetic modeling: Geophysics, **54**, 263–266.

Bannister, P. R., 1984, New simplified formulas for ELF subsurface-to-subsurface propagation: IEEE Journal of Oceanic Engineering, **OE-9**, 154–163.

Cagniard, L., 1953, Basic theory of the magneto-telluric method of geophysical prospecting: Geophysics, **18**, 605–635.

Chave, A. D., and C. S. Cox, 1982, Controlled electromagnetic sources for measuring electrical conductivity beneath the oceans, 1, Forward problem and model study: Journal of Geophysical Research, **87**, 5327–5338.

Chave, A. D., S. C. Constable, and R. N. Edwards, 1991, Electrical exploration methods for the seafloor, *in* M. Nabighian, ed., Electromagnetic Methods in Applied Geophysics, 2: SEG, 931–966.

Cheesman, S. J., R. N. Edwards, and A. D. Chave, 1987, On the theory of sea-floor conductivity mapping using transient electromagnetic systems: Geophysics, **52**, 204–217.

Constable, S., and C. S. Cox, 1996, Marine controlled source electromagnetic sounding 2. The PEGASUS experiment: Journal of Geophysical Research, **101**, 5519–5530.

Constable, S. C., C. S. Cox, and A. D. Chave, 1986, Offshore electromagnetic surveying techniques: 56th Annual International Meeting, SEG, Expanded Abstracts, 81–82.

Constable, S., A. Orange, G. M. Hoversten, and H. F. Morrison, 1998, Marine magnetellurics for petroleum exploration 1. A seafloor instrument system: Geophysics, **63**, 816–825.

Constable, S. C., R. L. Parker, and C. G. Constable, 1987, Occam's inversion: A practical algorithm for generating smooth models from electromagnetic sounding data: Geophysics, **52**, 289–300.
Cox, C. S., 1981, On the electrical conductivity of the oceanic lithosphere: Physical Earth Planetary International, **25**, 196–201.
Cox, C. S., J. H. Filloux, D. I. Gough, J. C. Larson, K. A. Poehls, R. P. Von Herzen, and R. Winter, 1980, Atlantic lithosphere sounding: Journal of Geomagntism of Geoelectricity, **32**, Suppl. I, SI 13–SI 32.
deGroot-Hedlin, C., and S. C. Constable, 2004, Inversion of magnetotelluric data for 2D structure with sharp resistivity contrasts: Geophysics, **69**, 78–86.
Eidsmo, T., S. Ellingsrud, L. M. MacGregor, S. Constable, M. C. Sinha, S. Johanson, F. N. Kong, and H. Westerdahl, 2002, Sea Bed Logging (SBL), a new method for remote and direct identification of hydrocarbon filled layers in deepwater areas: First Break, **20**, 144–152.
Ellingsrud, S., T. Eidsmo, S. Johansen, M. C. Sinha, L. M. MacGregor, and S. Constable, 2002, Remote sensing of hydrocarbon layers by seabed logging (SBL): Results from a cruise offshore Angola: The Leading Edge, **21**, 972–982.
Flosadottir, A. H., and S. Constable, 1996, Marine controlled source electromagnetic sounding 1. Modeling and experimental design: Journal of Geophysical Research, **101**, 5507–5517.
Hoehn, G. L., and B. N. Warner, 1983, Magnetotelluric measurements in the Gulf of Mexico at 20 m ocean depths, *in* R. A. Geyer, ed., CRC Handbook of Geophysical Exploration at Sea: CRC Press, 397–416.
Hoversten, G. H., S. Constable, and H. F. Morrison, 2000, Marine magnetellurics for base salt mapping: Gulf of Mexico field-test at the Gemini structure: Geophysics, **65**, 1476–1488.
Johansen, S. E., H. E. F. Amundsen, T. Røsten, S. Ellingsrud, T. Eidesmo, and A. H. Bhuyian, 2005, Subsurface hydrocarbons detected by electromagnetic sounding: First Break, **23**, 31–36.
Kong, F. N., H. Westerdahl, S. Ellingsrud, T. Eidesmo, and J. Johansen, 2002, 'Seabed logging': A possible direct hydrocarbon indicator for deepsea prospects using EM energy: Oil and Gas Journal, **100**, 30–38.
MacGregor, L., and S. Sinha, 2000, Use of marine controlled-source electromagnetic sounding for sub-basalt exploration: Geophysics Prosp., **48**, 1091–1106.
MacGregor, L., M. Sinha, and S. Constable, 2001, Electrical resistivity structure of the Valu Fa Ridge, Lau Basin, from marine controlled-source electromagnetic sounding: Geophysical Journal International, **146**, 217–236.
Røsten, T., and L. Amundsen, 2004, Generalized electromagnetic seabed logging wavefield decomposition into U/D-going components: 74th Annual International Meeting, SEG, Expanded Abstracts, 592–594.
Smith, T., M. Hoversten, E. Gasperikova, and F. Morrison, 1999, Sharp boundary inversion of 2D magnetotelluric data: Geophysical Prospectings, **47**, 469–486.
Spiess, F. N., K. C. Macdonald, T. Atwater, R. Ballard, A. Carranza, D. Cordoba, C. Cox, V. M. Diaz Garcia, J. Francheteau, J. Guerrero, J. Hawkings, R. Haymon, R. Hessler, T. Juteau, M. Kastner, R. Larson, B. Luyendyk, J. D. Macdougall, S. Miller, W. Normark, J. Orcutt, and C. Rangin, 1980, East Pacific Rise: Hot springs and geophysical experiments: Science, **207**, 142 1–1433.
Weiss, C. J., 2001, A matrix-free approach to solving the fully 3D electromagnetic induction problem: 71st Annual International Meeting, SEG, Expanded Abstracts, 1451–1454.
Wright, D. A., A. Ziolkowski, and B. A. Hobbs, 2001, Hydrocarbon detection with a multi-channel transient electromagnetic survey: 71st Annual International Meeting, SEG, Expanded Abstracts, 1435–1438.
Yuan, J., and R. N. Edwards, 2000, The assessment of marine gas hydrates through electrical remote sounding: Hydrate without a BSR?: Geophysical Research Letters, **27**, 2397–2400.